TENSILE TOUGHNESS TEST AND HIGH TEMPERATURE FRACTURE ANALYSIS OF THERMAL BARRIER COATINGS

G. QIAN[1], T. NAKAMURA[1], C. C. BERNDT[2] and S. H. LEIGH[2]

[1]Department of Mechanical Engineering and [2]Department of Materials Science and Engineering, State University of New York at Stony Brook, NY 11794, U.S.A.

Abstract—In this paper, an effective fracture toughness test which uses interface fracture mechanics theory is introduced. This method is ideally suited for determining fracture resistance of multilayered thermal barrier coatings (TBCs) consisting of ceramic and bond layers and, unlike other fracture experiments, requires minimal set-up over a simple tensile adhesion test. Furthermore, while other test methods usually use edge cracked specimens, the present test models a crack embedded within the coatings, which is more consistent with actual TBCs where failure initiates from internal voids or defects. The results of combined computational and experimental analysis show that any defects located within the ceramic coating can significantly weaken a TBC, whereas the debonding resistances of the bond coating and its interfaces are found to be much higher. In a separate analysis, we have studied fracture behavior of TBCs subjected to thermal loading in a high temperature environment. The computed fracture parameters reveal that when the embedded crack size is on order of the coating thickness, the fracture driving force is comparable to the fracture resistance of the coating found in the toughness test. In addition, the major driving force for fracture derives from the thermal insulating effect across the crack faces rather than the mismatch in the coefficients of thermal expansion. We have also investigated the effects of functionally graded material (FGM) within TBCs and found its influences on the fracture parameters to be small. This result implies that the FGM may not contribute toward enhancing the fracture toughness of the TBCs considered here. © 1997 Acta Metallurgica Inc.

1. INTRODUCTION

1.1. Thermal barrier coatings

The applications of materials in harsh environments or with stringent performance requirements call for advanced materials as well as technologies to improve the performance of existing materials. Of the latter category, coating technologies are among the most prominent and promising technologies that are being developed [1–3].

There are many coating methods that are currently being employed. Some common technologies are chemical vapor deposition, physical vapor deposition, atmospheric plasma spraying, vacuum plasma spraying and high velocity oxygen fuel processing (HVOF) [4]. Several of the above processing methods are categorized as thermal spray technology because a high temperature heat source is used to melt the intended coating materials. A laminate system of a NiCrAlY bond coat (0.13 mm thick) with an overlay of −0.40 mm yttria-stabilized zirconia (YSZ) has been used extensively in the aircraft industry to confer protection to turbine engine components. Such coatings are called "thermal barrier coatings" (TBCs) and they offer extended life to service-revenue aircraft or land-based power generating turbines by operation at high temperatures under corrosion environments [2].

Besides conventional materials, many new and more advanced materials are emerging for being used as coating materials. Among them, functionally graded materials (FGMs) have drawn attention because of unique and superior advantages over other materials in aerospace and high temperature applications [5, 6]. The concept of a FGM is to combine different materials during a well-controlled processing method, such as changing materials during spraying and/or chemical vapor deposition, to obtain the controlled variations of material properties for the newly-obtained material. Most often, the FGM can combine the superiority of each component material and phase out their inherent weaknesses.

1.2. Bonding strength—the fracture mechanics approach

For thermally sprayed coatings, debonding of the coating layer from a substrate or another coating, or cracking within a coating layer can lead to failure of the entire thermal coating system. In view of preventing mechanical failure, increasing the bonding strength directly benefits the integrity of the TBC. Furthermore, the bond strength is a very important design parameter used for lifetime estimates of the TBC. Thus, it is essential to establish an accurate bonding strength measurement of a given TBC or its resistance against fracture. One of the simplest and

most widely used methods to determine the bonding strength is to measure the critical tensile stress needed to cause separation within the TBC. In this method, the bond and ceramic coatings are sprayed over the top surface of a cylinder. Then an adhesive, usually epoxy, is applied and the TBC is bonded to another metal cylinder. This specimen is loaded to fracture by a tensile loading machine as shown in Fig. 1. This standardized method is described in ASTM C633-79 [7]. Such bond strength measurement is based on an initially defect-free assumption. However, in general, defects such as cracks, voids and oxidation of interfaces between splats may exist during the fabrication and service life of TBCs. In many cases, these defects cause stress concentration and weaken the adhesive linkage inside the coating system and, thereby, the critical tensile stress often overestimates the adhesive capacity of a practical coating system. Therefore, for the purpose of designing optimized TBCs, the fracture mechanics approach to measure bond strength is more suitable and provides a conservative debonding characteristic for the TBC.

There are already several methods of fracture toughness measurement. For example, the double cantilever beam (DCB) test [8], double torsion test, three point or four-point-bending test, scratch test [8] and Brazil-nut sandwich test [9] can measure fracture toughness. None of these testing methods is universal
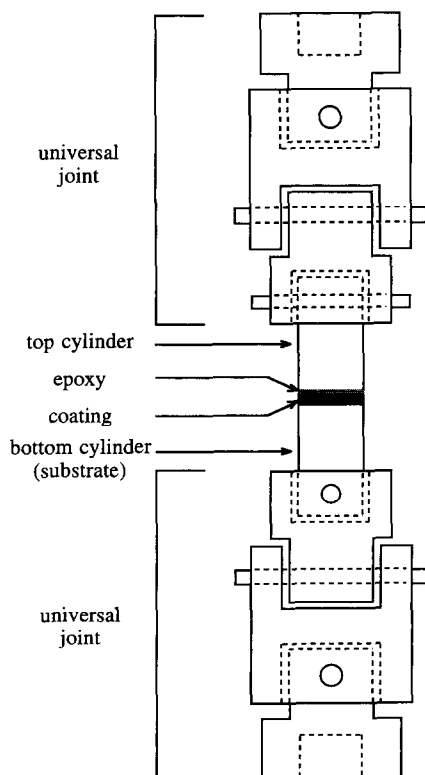

Fig. 1. Schematic of tensile toughness test assembly. The ceramic and bond coatings are sprayed on the bottom cylinder and bonded to the top cylinder with epoxy.

and applicable in every instance if the practical situation of application, cost of conducting the test and difficulties of implementation are taken into account. For instance, the DCB test is widely applicable to design engineers, but the complexity of specimen preparation and experimental techniques makes the test costly and time-consuming [8]. In the present work, a new type of fracture testing method is proposed which requires minimum specimen preparation and experimental set-up beyond the common adhesion test described earlier. Furthermore, most fracture tests are conducted with edge crack configurations and they may not represent the way cracks or defects are contained in coatings. Usually, these cracks are entirely embedded within coatings, and they are dissimilar to the edge cracks which are modeled in many fracture tests. This method also allows an initial defect to be located *anywhere* within the thermal barrier coating. Furthermore, in other fracture tests, the fracture or delamination plane is usually restricted to the interface between coating and substrate layers.

The complexity of conducting a fracture test such as the DCB test lies in treatment of the mixed-mode nature of the crack tip singularity field at an interface. Many interface and bimaterial fracture experiments of different structures have shown that the mixed-mode condition greatly affects the measurements of interface toughness. However, such an influence has been seldom considered in previous TBC fracture analyses. In this test, the complete interface fracture mechanics theory, which takes into account the mixed-mode or stretch-shear ratio of crack tip loading, is included in the analysis. Various mixtures of Modes I and II corresponding to opening and sliding of crack planes, respectively, are expected for different coating system configurations. Therefore, it is more illustrative and convenient to use the energy concept, namely, the critical energy release rate G_c, instead of the critical stress intensity factor of either Mode I or Mode II, K_{IC} or K_{IIC}, to quantify the fracture toughness. This approach has been used widely to measure interface toughness of bimaterial systems [10]. In many interface fracture tests, the critical energy release rate for fracture initiation was shown to be dependent upon the ratio of Mode I and Mode II stress intensity factors or the nondimensional phase angle. In general, a larger critical energy release rate was observed when a larger ratio of shear over tensile loading exists.

The key feature of the proposed fracture test is the axisymmetrical or so-called penny-shaped crack included in a common specimen used for the simple adhesion test. In this fracture test, the critical debonding force, and consequently, the critical mean normal stress is measured as in the case of the adhesion test. However, due to the presence of a penny-shaped crack, the test result shows a drop in the critical stress. The fracture toughness can be obtained by correlating the critical tensile stress with

the energy release rate tabulated from finite element calculations. The energy release rate and the decoupled stress intensity factors of Modes I and II are computed for various crack locations and lengths using modified energy and interaction integrals. The axisymmetrical geometry of the present model also eliminates any unknown three-dimensional effects which arise in plane strain or plane stress analysis.

1.3. High temperature applications

The coated materials are often used in elevated temperature environments. The mismatch in the coefficients of thermal expansion (CTEs) among different materials as well as the temperature gradient across the depth of coating can cause thermal stresses near cracks and voids. This type of singularity may cause the failure of TBCs in service. More importantly, an opened crack embedded in the coating can act as a thermal shield during the thermal loading and cause a temperature jump across the crack faces. Such a jump will dramatically increase the driving force for crack growth and make the TBC more susceptible to failure in high temperature applications. In this analysis, Ti–6Al–4V is used as the substrate material which is subjected to 1100°C. The yttria-stabilized zirconia (YSZ) coating bonded with NiAl experiences a temperature drop of 250°C across its thickness. The temperature distributions in the coatings with and without considering the effect of thermal insulation in a large crack model are analyzed and their numerical results are presented in Section 5.

2. FRACTURE TOUGHNESS TEST OF TBC

The proposed test method has two stages. In the first stage, a systematic computational analysis is performed for cracks embedded at different locations. In the analysis, the crack shape is assumed to be circular and a reference tensile load is applied perpendicular to the crack and the coating layers. In every model, energy release rate and mixed-mode stress intensity factors are calculated as the characterizing parameters for fracture toughness. These parameters are tabulated as reference values or geometrical factors for determination of critical fracture toughness in the next stage where actual experiments are carried out. In the second stage, a TBC specimen is prepared to contain a very weak bonding region which is assumed to simulate a circular embedded crack. In the experiment, a critical tensile load needed for failure is measured. Using the critical load and tabulated reference factors obtained in the first stage, the critical fracture parameters are determined for specimens containing cracks at different locations.

2.1. Experimental procedure

The proposed fracture test is developed by modifying a standard tensile adhesion test (TAT).

The standard test procedure according to ASTM 633-79 was found to have a nonuniform tensile stress over the cross-sections close to the coatings [11]. The revised specimens with a hole drilled in the radial direction were used in the modified TAT. The hole in the top cylinder is arranged 90° from the orientation of the hole in the substrate (Fig. 1). It was found the stress distribution in this set-up is nearly uniform (to within 2%) across the coating surface [12].

A layer of YSZ (ZrO_2-8wt.%Y_2O_3) was sprayed on top of the metallic bond coat (Ni-4wt.%Al) on the steel cylinder of 25.4 mm diameter and 40.0 mm length. The thickness of the zirconia coat (ceramic coating) and the bond coat are about 0.4 mm and 0.13 mm, respectively. During the process of thermal spraying, a very thin circular carbon layer, simulating a crack, is applied inside the coatings at about the center of the cylindrical face [13]. The carbon layer introduces an extremely weak internal interface and essentially, an embedded penny-shaped crack is created within the coatings. The diameter of the crack is set at 5 mm while its location within the TBC in terms of depth is varied for different models. After thermal spraying is completed, another steel cylinder of the same dimensions as the first is bonded to the ceramic coating using epoxy-based adhesive. The thickness of the epoxy layer is about 0.05 mm. The whole specimen is then inserted in the loading machine, shown in Fig. 1, for the uniaxial tensile test. The crosshead displacement is 0.013 mm/sec and when failure of the coating occurs, the corresponding applied force is recorded as the critical tensile load. The properties of materials used in the test are listed in Table 1. These values are also used for the input in the computational analysis.

In the experiment, fracture toughnesses of penny-shaped cracks at three geometrically significant locations are investigated, as shown in Fig. 2. They are (1) crack between ceramic and bond coatings; (2) crack within ceramic coating; and (3) crack between bond coat and substrate. In the figure, depth d for each crack is measured from the boundary of the ceramic coating and the epoxy layer. (Note: a model with a FGM layer is also shown in Fig. 2 and will be discussed in Section 3.4.) The fracture toughness results using the current test method are described in Section 4.

2.2. An interface fracture mechanics approach

The coating model considered here is not defect-free. It contains an artificially introduced

Table 1. Material properties of specimen

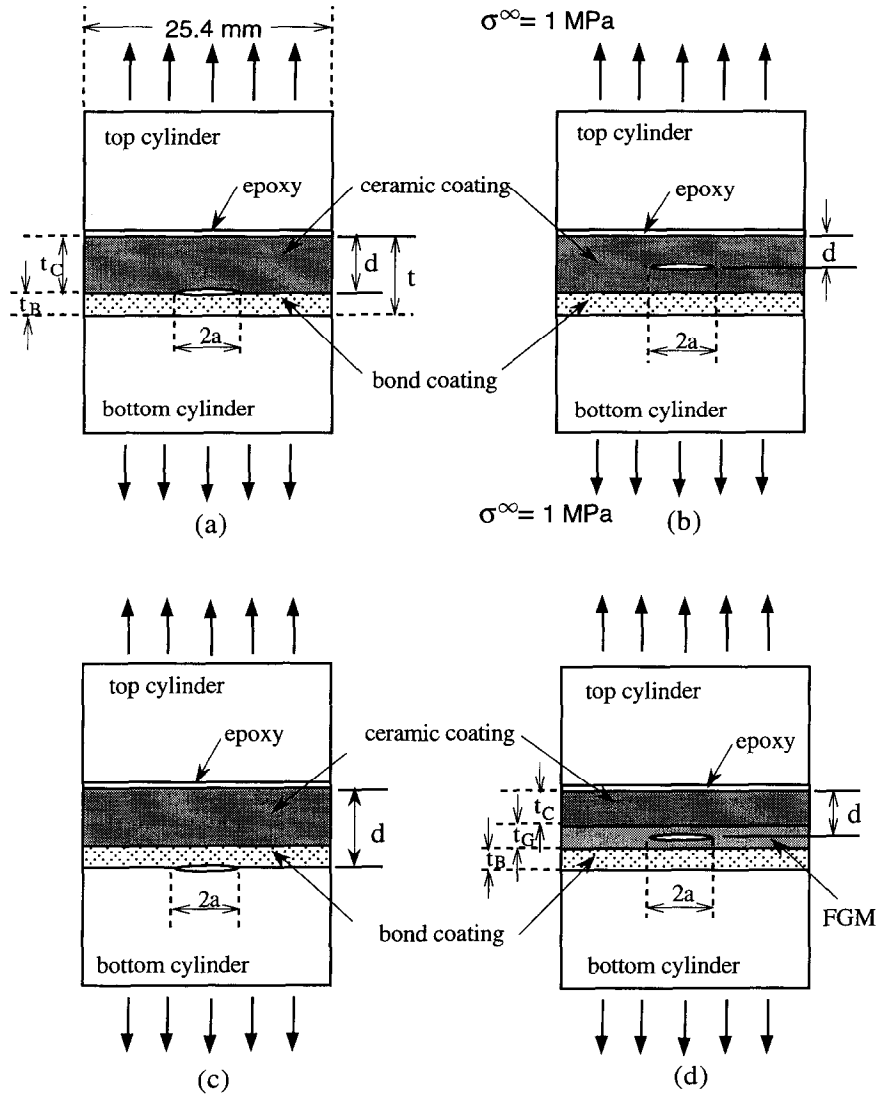| Materials	E	v	CTE
YSZ (ceramic coating)	50 GPa	0.25	10.0×10^{-6}/C
NiAl (bond coating)	30	0.25	~14.0
steel (top and bottom cylinders)	200	0.30	12.0
Ti6Al4V (substrate)	110	0.30	10.5
epoxy (adhesive)	1.5	0.35	N.A.

Fig. 2. Various locations of initial embedded cracks shown in the cross-sections of axisymmetric models. Tensile loading is assumed to be $\sigma^\infty = 1$ MPa. The coating thickness, the crack size and the cylinder diameter are not drawn in scale. (a) Interface crack between the ceramic and bond coatings. (b) Homogeneous crack within the ceramic coating. (c) Interface crack between the bond coating and the substrate (bottom cylinder). (d) Crack in the functionally graded material.

penny-shaped crack somewhere inside the coating which is subjected to a far-field uniaxial tension. From the fracture mechanics point of view, some energy must be used to create new crack surfaces. Consequently, the energy release rate, more precisely defined as the energy released per unit area of free crack surfaces, is the "driving force" behind crack propagation. In terms of defining toughness of material, a critical value of energy release rate can be used as the fracture resistance. In linear elastic fracture mechanics (LEFM), the energy release rate G is equivalent to the path-independent J-integral. To facilitate the evaluation of G in the finite element analysis, it is represented as a domain integral [14]. The thermal stress terms are also included for

the high temperature analysis and the integral for axisymmetric problems is shown as,

$$
G = \frac{1}{a} \int_A \left\{ \left[\sigma_{\beta\gamma} \frac{\partial u_\beta}{\partial r} - W\delta_{r_i} \right] r \frac{\partial q}{\partial x_i} \right.
$$

$$
\left. + \left[\sigma_{\theta\theta} \frac{u_r}{r} - W + \alpha\sigma_{kk} \frac{\partial T}{\partial r} r \right] q \right\} dA \quad (1)
$$

Here a is the radius of crack, W is the mechanical part of strain energy density given by $W = (\sigma_{ij}\epsilon_{ij} - \alpha T\sigma_{kk})/2$, α is the coefficient of thermal expansion (at a material point where the integrand is evaluated), q is a weighting parameter and T is the temperature deviation from a reference value at the undeformed

state. The indices β and γ range over r and z, respectively and $x_r = r$ and $x_z = z$. The detailed implementation of the above integral in the finite element analysis can be found in [15].

One of the most important features of an interface crack is the mixed-mode nature of the near-tip singularity field. Even under far-field tension, the crack tip (or crack front in the axisymmetric case) field contains shear loading due to the mismatch in the elastic properties of two adjoining materials. Namely, a pure Mode I or pure Mode II stress is generally not observed for an interface crack problem and both K_I and K_{II} exist. Here, K_I and K_{II} are the stress intensity factors of Modes I and II, respectively. The relation between the energy release rate and the coupled stress intensity factors of difference modes is given as:

$$G = \frac{1}{E^* \cos \mathrm{h}^2(\pi\epsilon)}(K_I^2 + K_{II}^2) \tag{2}$$

where E^* is the effective Young's modulus and it is defined as,

$$\frac{2}{E^*} = \frac{1}{E_1} + \frac{1}{E_2},$$

$$\overline{E_\alpha} = E_\alpha \text{ for plane stress,}$$

$$\overline{E_\alpha} = \frac{E_\alpha}{1 - \nu^2} \text{ for plane strain} \tag{3}$$

Mode II and Mode I stress intensity factors as shown above. In this analysis when the crack is on the interface (e.g. between ceramic and bond coatings), the characteristic length L is chosen to be 100 μm in reporting the phase angle. For cracks in a homogeneous medium (e.g. entirely within ceramic coating), the oscillatory index is zero and the phase angle is exactly the angle ratio between K_{II} and K_I. In either case, the phase angle is used to measure relative magnitudes of shear and tensile loads near the crack. If large tension or opening mode exists, the phase angle is $\psi = 0°$, while $\psi = 90°$ or $-90°$ when shear loading is dominant. To determine the phase angle, the stress intensity factors of Modes I and II need to be computed. In order to extract them from the computed stress field, an auxiliary field corresponding to a known asymptotic solution [17] is superimposed on the actual field. The difference in the energy release rate of the total field and the sum of the actual field and the auxiliary field is termed as the interaction energy release rate, and it contains the information related to the stress intensity factors of the actual field. The interaction energy can be also represented in the form of a domain integral for axisymmetric problems [18]. Here, this integral is modified to include the thermal stress loading condition as:

$$I = \frac{1}{a}\int_A \left\{\left[\sigma_{\beta\gamma}\frac{\partial u_\beta^{\mathrm{aux}}}{\partial r} + \sigma_{\beta\gamma}^{\mathrm{aux}}\frac{\partial u_\alpha}{\partial r} - \sigma_{\kappa\eta}\epsilon_{\kappa\eta}^{\mathrm{aux}}\delta_{r_z}\right]r\frac{\partial q}{\partial x_z} + \left[\sigma_{\theta\theta}^{\mathrm{aux}}\frac{u_r}{r} + \sigma_{\theta\theta}\frac{u_r^{\mathrm{aux}}}{r} - \sigma_{\kappa\eta}\epsilon_{\kappa\eta}^{\mathrm{aux}}\right]q \right.$$

$$\left. + \left[\sigma_{\beta\gamma}^{\mathrm{aux}}\frac{\partial u_z}{\partial r} - \sigma_{\theta\theta}^{\mathrm{aux}}\frac{\partial u_r}{\partial r} + \sigma_{\theta\theta}\left(\frac{\partial u_r^{\mathrm{aux}}}{\partial r} - \frac{u_r^{\mathrm{aux}}}{r}\right) + \alpha\sigma_{kk}^{\mathrm{aux}}\frac{\partial T}{\partial r}r\right]q\right\}\mathrm{d}A \tag{5}$$

Here the subscript $\alpha = 1$ indicates the material above the crack while $\alpha = 2$ indicates the material below the crack. The asymptotic near-front K-field of axisymmetric cracks is equivalent to that of plane strain cracks.

The relative value of each stress intensity factor at a crack tip plays an important role in the initiation of crack growth for an interface crack as well as for a homogeneous crack subjected to a mixed-mode loading condition. It is convenient to define their relative magnitudes in terms of a nondimensional phase angle. When the oscillatory index ϵ of an interface is non-zero, it must be defined with the characteristic length L. Mathematically, it is an angle ratio of the imaginary and real parts of the complex stress intensity factor K multiplied with $L^{\mathrm{i}\epsilon}$ [16].

$$\psi = \tan^{-1}\frac{\mathrm{Im}(KL^{\mathrm{i}\epsilon})}{\mathrm{Re}(KL^{\mathrm{i}\epsilon})} \approx \tan^{-1}\frac{K_{II}}{K_I} \tag{4}$$

Here $K = K_I + iK_{II}$ and i is an imaginary number. This phase angle essentially represents the ratio of

where the superscript "aux" indicates the auxiliary field. All the other quantities are those of the actual field. The interaction energy release rate is related to the stress intensity factor of the actual field as:

$$I = \frac{E^*}{2\cos\mathrm{h}^2(\pi\epsilon)}(K_I K_I^{\mathrm{aux}} + K_{II}K_{II}^{\mathrm{aux}}) \tag{6}$$

Where the complex stress intensity factor of the auxiliary field is of the form $K^{\mathrm{aux}} = K_I^{\mathrm{aux}} + iK_{II}^{\mathrm{aux}}$. If an auxiliary field with a unit stress intensity factor $K^{\mathrm{aux}} = 1$ is superimposed on the actual field, K_I of the actual field can be extracted from (6) after the interaction energy release rate I associated with this auxiliary field has been evaluated. Similarly, if an auxiliary field with a unit stress intensity factor $K^{\mathrm{aux}} = i$ is superimposed on the actual field, K_{II} of the actual field can be extracted. Then, the phase angle can be calculated from (4).

The energy release rate as well as the mixed-mode stress intensity factors can be calculated from (1) and (6), respectively, for different crack locations and

sizes. On the basis of these calculated results, the fracture toughness and the corresponding phase angle can be determined from the critical debonding stress measured in the experiment.

3. COMPUTATIONAL ANALYSIS

3.1. Computational model

The 4-node bilinear isoparametrix axisymmetric elements are used to construct the finite element model. Since a large number of different models must be analyzed, a mesh generator code was developed. A typical mesh which depicts the specimen is shown in Fig. 3. The mesh becomes denser in the area surrounding the crack tip. A specially refined crack

tip mesh which occupies a small rectangular area (10×10 μm) around the crack tip is adopted because of the expected high stress gradient. In this region, 16 singular crack tip elements are employed. Furthermore, small elements are placed along the boundaries of different coating layers to accurately capture large strain changes caused by the material mismatch. The total of 2000–3000 elements are used in each axisymmetrical model.

As discussed in Section 2.1, three primary crack locations are investigated in this analysis. In the initial study, the functionally graded material is not included in the analysis. The FGM is modeled in the subsequent computational analysis to understand the effect of graded materials in TBC's. We note that the
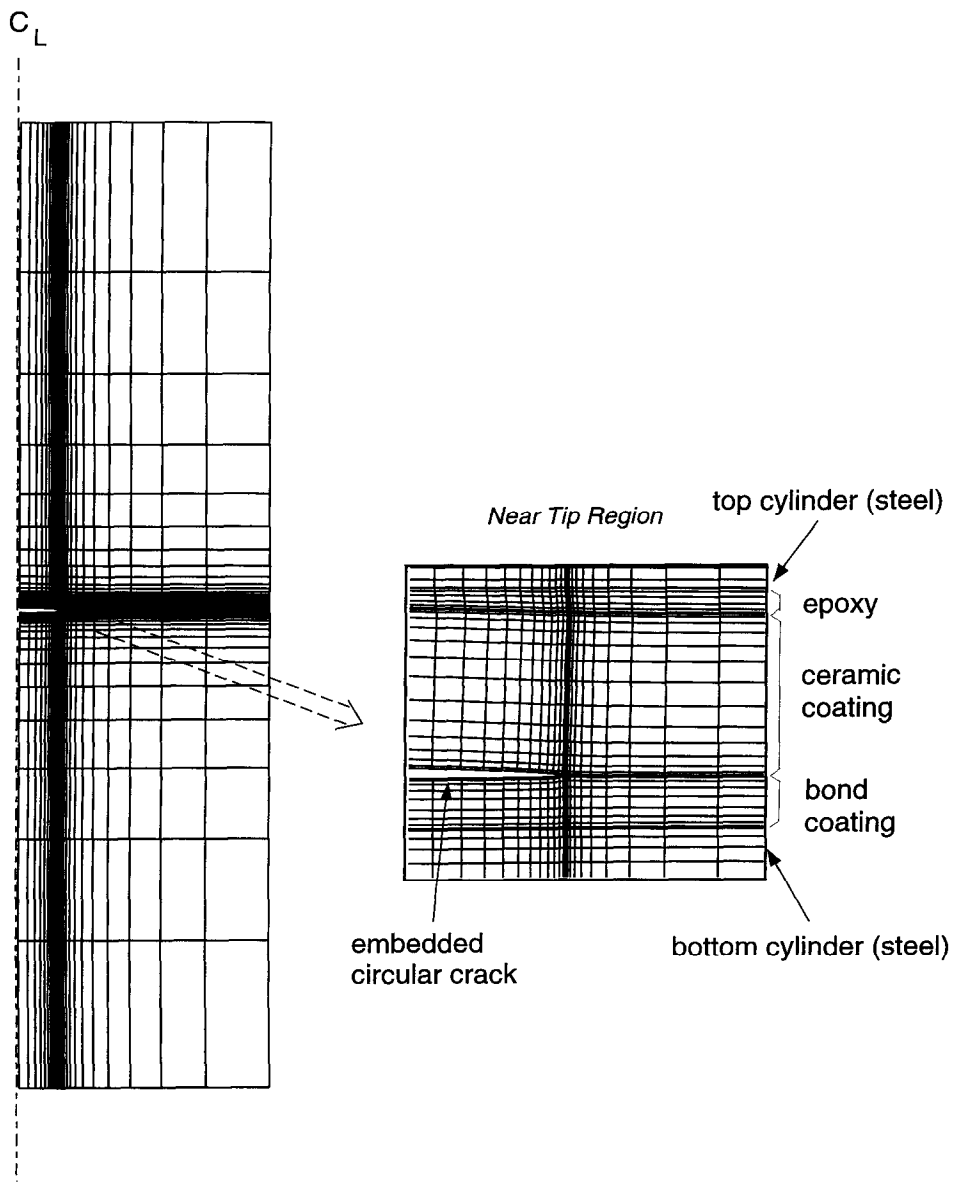

Fig. 3. A typical axisymmetrical finite element mesh of specimen with an interface crack between ceramic and bond coatings. Near crack tip region is enlarged and different layers are noted.

effect of FGM is only investigated in the finite element analysis and specimens with a FGM layer are not experimentally tested.

3.2. Cracks inside TBC under uniaxial load

Initially, the models with different crack locations shown in Figs 2(a)–(c) are investigated with the finite element method. Each model contains a total of five layers; top steel cylinder, adhesive epoxy, ceramic coating, bond coating and bottom steel cylinder. For the top and bottom cylinders, each layer thickness is always set as 20 mm, which is sufficiently large to eliminate any thickness effect of the cylinders. For the epoxy which is used to bond the top cylinder to the surface of the ceramic, its thickness is assumed to be 50 μm. The effect of the epoxy layer on the coating system will be discussed in the next section. For the two sprayed coating layers, the thicknesses are set to 400 μm and 130 μm for the ceramic and bond coatings, respectively. These are typical values for the actual coatings used in the TAT experiment. Although not reported here, calculations show that a small variation in the coating thickness has a minimum effect on the energy release rate and the phase angle. The depths of three different cracks are measured from the epoxy-ceramic coating boundary and given as $d = 0.2$, 0.4 and 0.53 mm, respectively. The shallowest depth corresponds to the crack at the middle of the ceramic coating (Fig. 2(a)). The second depth corresponds to the case of the interface crack on the boundary between the ceramic and bond coatings (Fig. 2(b)). The third depth is for the interface crack between the bond coating and the bottom cylinder/substrate (Fig. 2(c)). For each model, computations are carried out for at least 10 different crack radii, ranging from $a = 0.1$ mm to 4 mm. In every calculation, the energy release rate and the mixed-mode stress intensity factors are obtained using (1) and (6). The reference tensile stress is set at $\sigma^{\infty} = 1$ MPa in all cases. Note that the energy release rate varies proportional to the square of the tensile stress while the phase angle is independent of the magnitude of tensile stress.

The computed results in Fig. 4(a) show that the energy release rate of each model increases with the crack radius. In fact, the increasing behavior of G is very similar in all cases and the differences are very small for large cracks. This result is consistent with available analytical solutions for a long crack in layered plates (e.g. adhesive joint). However for small cracks ($a < 1$ mm), a greater spread among the three cases can be observed. At $a = 0.5$ mm, the energy release of the crack embedded within the ceramic coating is nearly twice as large as that of the interface crack between the ceramic and bond coatings.

The phase angles are also computed from the extracted Mode I and II stress intensity factors and shown in Fig. 4(b). Essentially, the results illustrate the dominant tensile mode; i.e. $\psi \approx 0°$, for all the cases due to the nature of the loading condition. Any
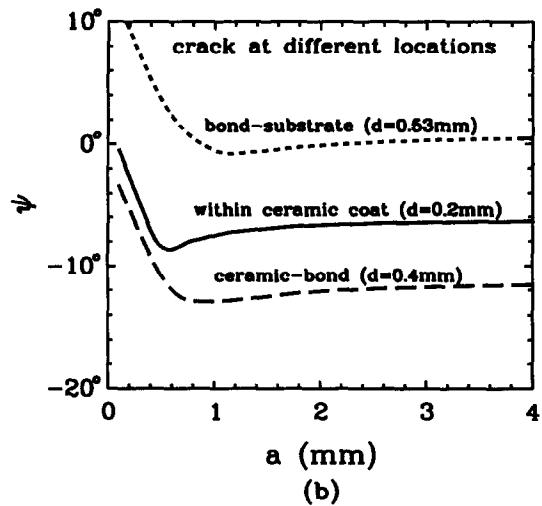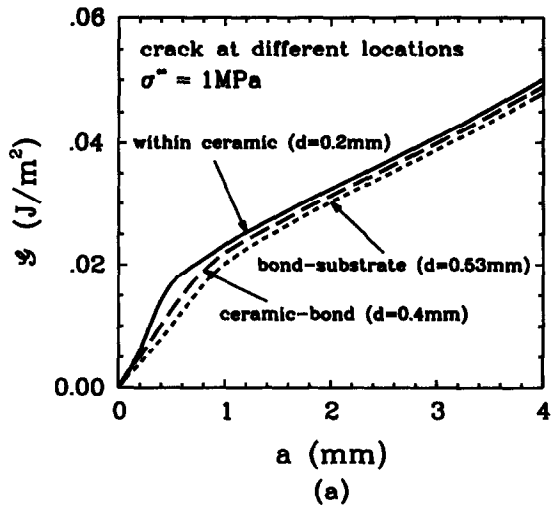

Fig. 4. (a) Energy release rate as a function of embedded crack radius for cracks at different locations. The specimens are under tensile pressure of 1 MPa. (b) Corresponding phase angle.

contribution to shear loading arises purely from the mismatch in the material properties. Initially the phase angle decreases with increasing crack size. But as the crack size exceeds the thickness of coating ($t = 0.53$ mm), the phase angle approaches a steady state value for each model. The largest shear mode appears in the case for the interface crack between the ceramic and bond coatings.

3.3. Effects of epoxy layer

The effects of the adhesive epoxy layer (used to bond the TBC to the top steel cylinder) are examined here. Since the thickness of the epoxy layer is usually a small fraction of the thickness of the coating layer, such an effect had been assumed to be minimum. However, a further analysis shows that this effect can be important due to its significantly low modulus compared to the moduli of other materials used in the test. Here the results are only presented for cracks

located between the ceramic and bond coatings. The other models with different crack locations also show similar epoxy effects. Three different thicknesses of epoxy layers are considered. They are, one with no epoxy ($t = 0$), another one with a typical thickness ($t = 50\ \mu$m, the results already shown in Fig. 4) and the last one with a thicker layer ($t = 100\ \mu$m). The computed results, Fig. 5(a), show that the energy release rate increases significantly as the epoxy layer becomes thicker. In fact, nearly a 100% increase in G is observed from the 100 μm thick model over the one without any epoxy layer. However, note that for a very small crack (i.e. $a < 0.2$ mm), the results are nearly identical. The differences only increase as the crack diameter approaches the total coating thickness and the *relative* differences become fixed after the steady state is reached for $a > 1$ mm. The computed phase angles in Fig. 5(b) also indicate sizeable

Fig. 6. Variations of material constants through thickness is illustrated for the model with functionally graded material (FGM).
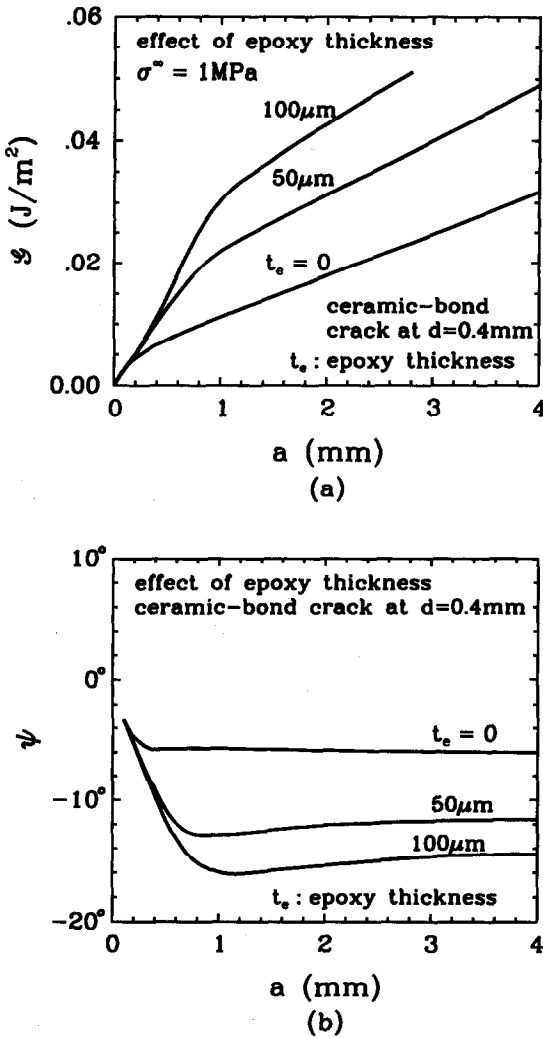

Fig. 5. (a) Energy release rate as a function of embedded crack radius for different epoxy layer thickness. The results are shown for the interface crack between the ceramic and bond coatings. (b) Corresponding phase angle.
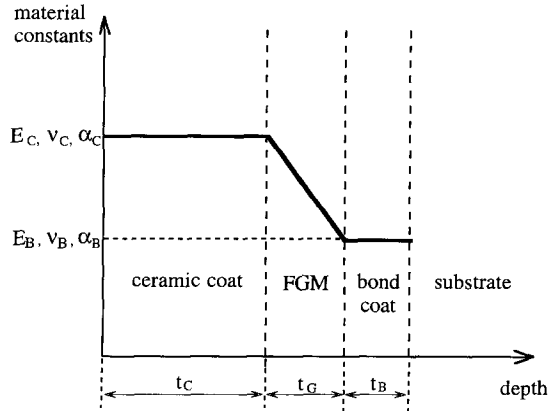
differences in the three models. A greater Mode II contribution (i.e. larger absolute value of ψ) is observed for larger epoxy layer thicknesses. This result implies more shearing force is present near the crack front when a thick epoxy layer is present. In fact, when the thickness of the epoxy layer increases from 0 to 100 μm, K_I increases only about 10%, but K_{II} increases about 50%. This shows that the large increase in the energy release rate is attributed to the significant rise in the Mode II loading.

These results suggest that the effects of epoxy layer can be significant and one must be careful in applying the adhesive epoxy layer during preparation of specimens. Alternatively, it may be feasible to control the ratio of tension to shear loading at the crack front or change the phase angle by choosing a suitable thickness for epoxy. Such a technique may be useful to create a mixed-mode loading condition similar to the one found in a high temperature environment (discussed in Section 5). Other calculations have shown that the effects of epoxy layer can be significantly reduced if an adhesive with a higher Young's modulus is used.

3.4. Functionally graded interface

Although not used in the experiment, the effects of functionally graded material (FGM) are studied in the computational analysis using the model shown in Fig. 2(d). The FGM eliminates a distinct interface between the ceramic and bond coatings and earlier studies have shown smaller stress concentration to occur near flaws and cracks in the FGMs due to elimination of material mismatch [19]. For the current analysis, the material properties within the FGM region are assumed to vary linearly with thickness as shown in Fig. 6. In order to include this FGM in the finite element model, a set of discrete heterogeneous materials whose properties vary across element layer is used (i.e. E and v change element by element). Note that even in the actual coatings, the variation of material properties can only occur at the

Table 2. Critical tensile stress (σ_C^x) measurements

initial crack at ceramic–bond		initial crack within ceramic		Initial crack at bond–substrate	
specimen #1	4.85 MPa	specimen #5	5.07 MPa	specimen #8	5.55 MPa
specimen #2	5.70	specimen #6	5.23	specimen #9	5.76
specimen #3	6.16	specimen #7	5.25	specimen #10	7.06
specimen #4	4.17				
average σ_C^x	5.22 MPa	average σ_C^x	5.19 MPa	average σ_C^x	6.12 MPa

level of splat sizes[1].† In the computational model, the thickness of each element layer is chosen to be 5 μm, which is close to a typical thickness of a splat. The total thickness of FGM is assumed to be $t_G = 100$ μm and 20 element layers with gradually changing material properties are employed. In addition, the embedded crack is assumed to be located at the mid-point of the FGM at $d = 0.4$ mm. Since FGM is placed at the middle of the ceramic and bond coats, the thicknesses of the ceramic and bond layers are reduced to be 0.35 mm and 0.08 mm, respectively.

The computed energy release rate of the crack within the FGM under the tensile load of $\sigma^x = 1$ MPa is shown in Fig. 7(a). For comparison, the result of the ceramic–bond interface crack ($t_G = 0$) at the same depth location is also plotted in the figure. The two results show almost no difference in G. A somewhat larger difference is observed for the phase angle shown in Fig. 7(b). As expected, the FGM reduces the magnitude of phase angle or the shear effect due to the material mismatch. The effects of FGM are also investigated in a high temperature environment, where small thermal stresses may prevail in the FGM because of the smooth transition in the material properties. This analysis is described in Section 5.

4. EXPERIMENTAL RESULTS

A total of ten tests were conducted according to the procedure outlined in Section 2.1. During fabrication of each specimen, an extremely thin carbon layer with circular radius of $a = 2.5$ mm was applied within the TBC. These specimens are loaded to fracture and the corresponding critical stresses are recorded. In Table 2, the tensile loads needed to fracture three types of models are listed. Photographs of fractured specimens, one from each model, are shown in Fig. 8. The failure patterns observed from these specimens are also illustrated in Fig. 9 for the three different initial crack locations. These patterns have a common morphological feature, i.e. all primary failures eventually occur within the ceramic coating regardless of the initial crack locations. From the average critical tensile stress σ_C^x for each model listed

in Table 2, the corresponding energy release rate and the Mode I and II stress intensity factors are determined by converting the computed data shown in Fig. 4 (G is proportional to the square of σ^x while K_I and K_{II} are linearly proportional to σ^∞).

For the specimen with an initial crack along the interface of the ceramic and bond coatings, the picture in Fig. 8(a) shows the initiation of crack propagation at the initial crack. However, the crack
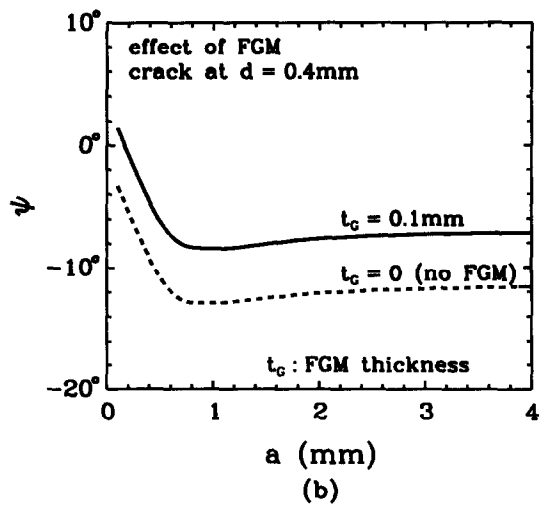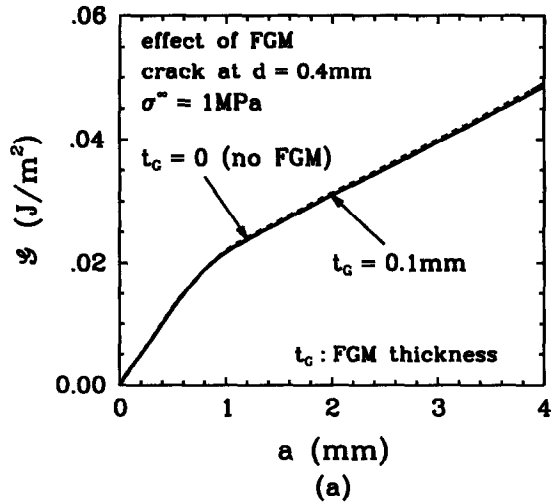

Fig. 7. (a) Energy release rate as a function of embedded crack radius for the FGM crack. The result of the interface crack between the ceramic and bond coatings (same depth location, but without FGM) is also shown for reference. (b) Corresponding phase angle.

†A "splat" is the prime microstructural feature that is exhibited in thermal spray deposits. A splat has the morphology of a "saucer" (or pancake) which cools down and condenses as a whole after it has been sprayed on an underlying material. A coating system is made of numerous splats ($\sim 2 \times 10^6$ per cm^3) which pile up on each other.
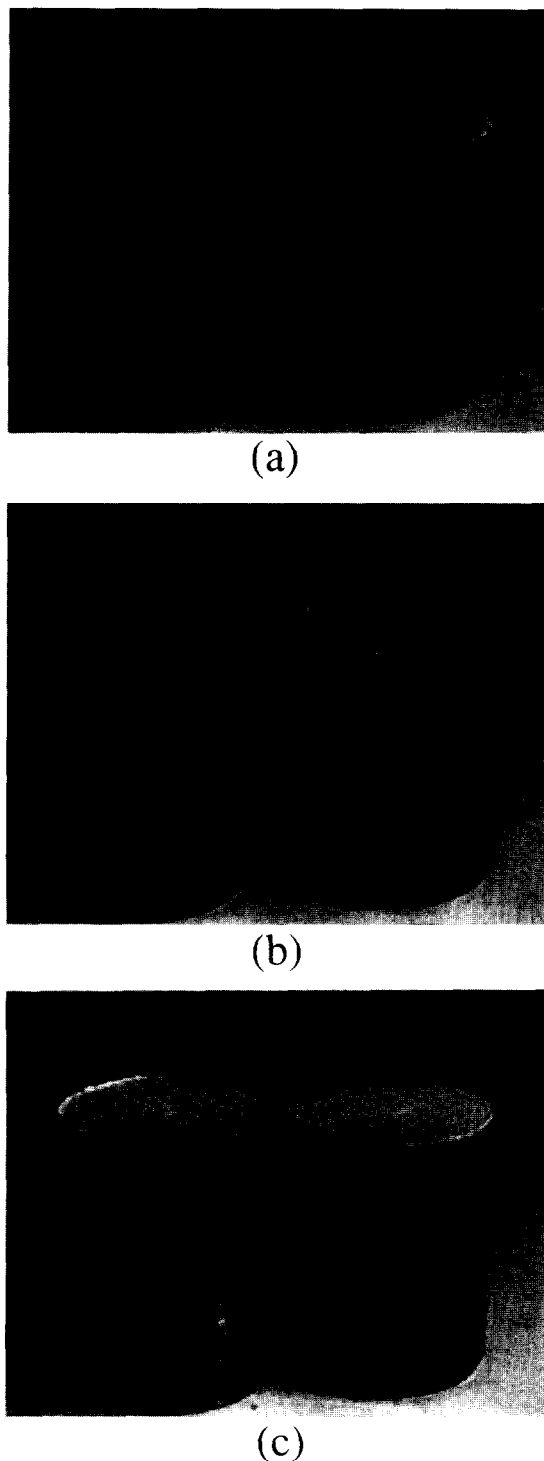
(a)

(b)

(c)

Fig. 8. Photographs depicting fractured surfaces of various broken specimens (with each top cylinder shown on the left). Dark circular regions near the center represent a thin carbon layer applied within coatings to simulate an initial crack. (a) Initial crack on the ceramic and bond coating interface. Uneven surfaces around the carbon layer indicate crack kinking after fracture initiation. (b) Initial crack within the ceramic coating. Flat surfaces, including the carbon layer, indicate planar fracture growth. (c) Initial crack on the bond coating and substrate interface. Fracture occurs entirely within the ceramic coating and ignores the embedded carbon layer.

immediately kinks away from the interface and propagates within the ceramic layer as described by the concave–convex surfaces with the visible dark carbon layer at the center. This failure path suggests that although a flaw on the interface can act as a source of crack initiation, the subsequent propagation must occur in the ceramic layer as illustrated in Fig. 9(a). This crack kinking can be attributed to the relatively large toughness of the interface of YSZ and NiAl as compared to that of YSZ. In other words, the crack requires less energy to propagate through the YSZ layer than along the interface. An interface crack kinking away from the bimaterial boundary was studied by He and Hutchinson [20]. According to their analysis, when a crack kinks into a stiffer material (i.e. YSZ, see Table 1), the material must be less tough than the interface. In addition, their analysis predicts that when the phase angle at the onset of kinking is approximately $\psi = -12°$ (from Table 3), the initial kink angle (i.e. the angle between the kinked crack and the interface) must be very small. Here, a close inspection of the fractured specimen confirms the very small kink angle, and in fact, the crack appears to "curve" out of the interface. The four tests conducted for this model have shown a large variation of σ_C^∞, perhaps because of the complicated kinking mechanism. Since the kinking occurs at the initiation, the critical fracture parameters shown in Table 3 should not be treated as regular fracture toughness values.

The second photograph in Fig. 8(b) depicts planar fracture surfaces of a specimen where the initial crack is in the ceramic. This model has the cleanest crack initiation and growth as shown by its failure path in Fig. 9(b). This is also evident from the small variation in the critical stresses listed in Table 2. The consistent measurements also validate the effectiveness of the carbon layer to act as an embedded crack. From the average critical stress, the fracture toughness or debonding strength of the YSZ coating is determined to be about $G_c = 1.0$ J/m^2 with $\psi = -6.5°$, as shown in Table 3.

In the third model where the initial crack is on the interface of the bond coating and the substrate, the failure did not initiate from the pre-existing crack. This is obvious from the picture in Fig. 8(c) where fractured surfaces do not contain dark circles corresponding to the carbon layer. Indeed the fracture occurred entirely within the ceramic layer as illustrated in Fig. 9(c). Such behavior implies that the bond–substrate interface is much tougher than that of the ceramic, and any flaws on this interface play no role in the fracture process of the TBC. A large variation in σ_C^x can be attributed to the fact that failure of a TBC requires spontaneous fracture initiation with the ceramic layer. Such a variation and the range of magnitudes are similar to those observed in tensile adhesion tests without initial crack. Since propagation did not initiate at the initial crack, the energy release rate as well as the stress intensity
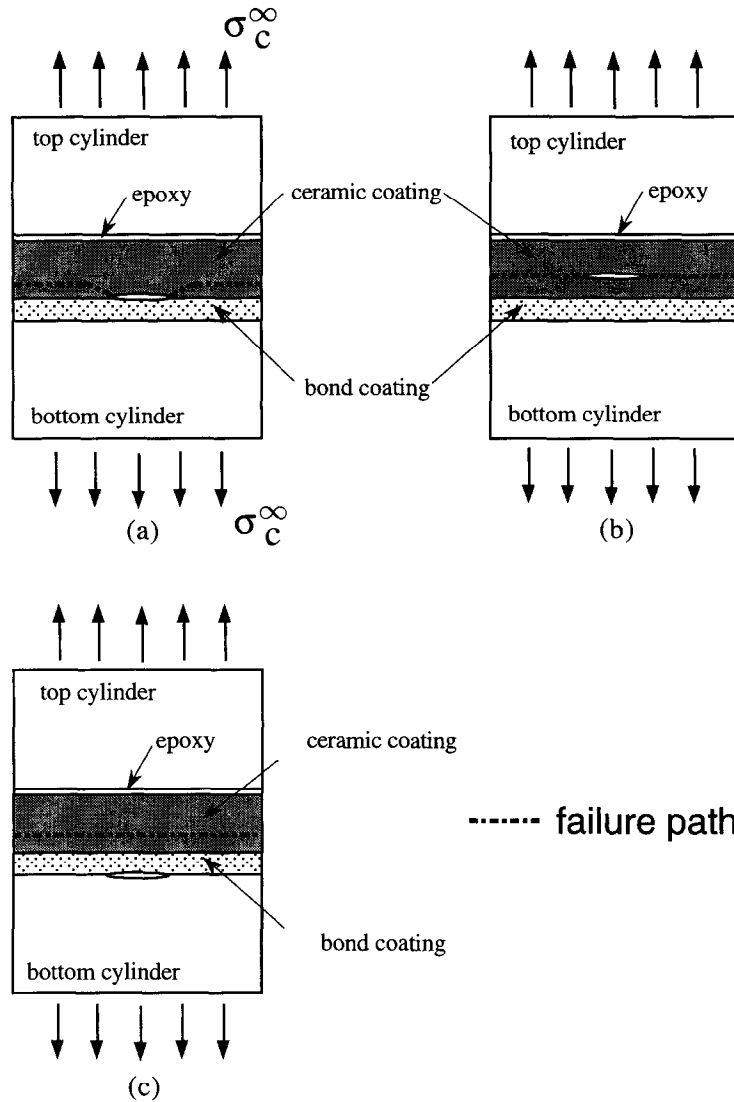
Fig. 9. Various failure paths are illustrated in the cross-sections of the specimens. (a) Propagation starts at the ceramic–bond interface, but the crack kinks into the ceramic coating and remains there. (b) Propagation starts at the embedded crack and continues inside the ceramic coating. (c) Initiation and propagation occur within the ceramic coating, disregarding the embedded crack on the interface of the bond coating and the substrate.

factors shown in Table 3 are by no means the fracture toughness of this interface. They simply represent the fracture parameters of the interface crack when failure occurs elsewhere.

In the current coating model, there are four physically distinguished locations. They are the ceramic coating, the interface of the ceramic–bond coatings, the bond coating and the interface of bond coating–substrate. Our experimental results clearly show the weakest location to be the ceramic coating. The bond coat made of sprayed NiAl shows a significant failure strength within itself as well as its

Table 3. Corresponding fracture parameters from average σ_c^∞ (crack radius: 2.5 mm)

Fracture parameters	Initial crack at ceramic–bond*	Initial crack within ceramic	Initial crack at bond–substrate**
G_C	0.966 J/m²	0.987 J/m²	1.29 J/m²
ψ	−11.9°	−6.53°	0.11°
K_{Ic}	0.193 MPa·m¹ᐟ²	0.228 MPa·m¹ᐟ²	0.277 MPa·m¹ᐟ²
K_{IIc}	−0.041 MPa·m¹ᐟ²	−0.026 MPa·m¹ᐟ²	0.0005 MPa·m¹ᐟ²

*Crack kinked away from the ceramic–bond interface.
**Failure did not initiate from the bond–substrate crack.

two adjacent interfaces. In other words, any failures are likely to occur within the YSZ coating and any enhancement of fracture resistance must be accompanied by an increase of YSZ toughness. This implication may reduce usefulness of a functionally graded material which is used to eliminate the ceramic and bond coating interface.

5. HIGH TEMPERATURE ANALYSIS

In many applications, thermal spray coatings are designed to function as a thermal shield to protect base structures from high temperatures. In such an environment, TBCs can break down due to thermal stresses generated by the CTE mismatch and/or temperature gradient through thickness. In this section, we have carried out a detailed fracture analysis of TBCs subjected to an elevated temperature. The thermal loading in TBCs has been studied by several investigators. Kokini [21] has shown the effect of strain mismatch caused by transient thermal loads. A temperature field and resulting thermal stresses have also been determined for functionally graded ceramic coatings [22]. Recently, Hutchinson and Lu [23] have shown that a thermal insulation across opened crack faces within a coating can cause significant increase in the crack driving force. Essentially, the insulation introduces a temperature jump across the crack faces while the temperature variation through thickness remains continuous outside the crack. Here, we have determined temperature fields in TBC models containing embedded cracks with the effect of thermal insulation across the crack surfaces.

In this analysis, the substrate is assumed to be Ti–6Al–4V alloy, often used for gas turbines, instead of the previous steel substrate. For the coating model, the same materials, YSZ and NiAl, with the same thicknesses are used. The environmental temperature at the coating surface is set at $T_{env} = 1100°C$ while a temperature drop of 250°C over the coating thickness of 0.53 mm is assumed. We have ignored any transient effect and no convection or radiation is considered. The substrate is modeled as a thermal sink, and a constant temperature $T_{sub} = 850°C$ always prevails at the bond–substrate interface. Axisymmetrical finite element models similar to the ones used in the previous analysis are constructed for this investigation. However, only the coatings and the bottom cylinder/substrate are modeled and the top cylinder and the epoxy layer are not included. In addition, loading to the crack is entirely from the thermal stresses generated by the steady-state high temperature field and no external mechanical load is applied. In the following sections, brief derivations of the temperature fields outside and inside a crack region are shown. The calculated temperature field is used as the initial condition in the finite element analysis.

5.1. Temperature profiles outside crack region

Under steady state condition, the heat flux q over any cross section of the coatings parallel to the layers must be constant and can be described by the following formulae,

$$q = -K_C\left(\frac{dT}{dz}\right)_C = -K_B\left(\frac{dT}{dz}\right)_B \qquad (7)$$

where K_C and K_B are the thermal conductivities of the surface ceramic coating and the bond coat, respectively. The positive z-axis is perpendicular to the coating layers and directed downwards. Thus, positive heat flow occurs along the z-direction. From a handbook [24], the thermal conductivities of YSZ and NiAl are determined as 1.5 W/(m·K) and 22.5 W/(m·K), respectively. These are bulk material properties and the actual values for sprayed coatings which contain voids are probably smaller. However, we note that as long as the ratio of the two, namely $K_B/K_C = 1/15$, remains constant, the temperature field determined in this derivation is unchanged. Within each layer, the temperature drops linearly with the depth, and the slope of temperature drop in the ceramic coating is 15 times that of the bond coat. Suppose we denote k_1 as the slope of temperature drop inside the bond coat, then $\Delta T_C = k_1 K_B t_C/K_C$, $\Delta T_B = k_1 t_B$. Here t_C and t_B are the thicknesses of the ceramic and bond coatings, respectively, and $t_C = 0.4$ mm and $t_B = 0.13$ mm. Also, $\Delta T = \Delta T_C + \Delta T_B = 250°C$ is the total temperature drop over the entire coatings while ΔT_C and ΔT_B are the temperature drops in the ceramic and bond coatings, respectively. One can solve for k_1 and determine $\Delta T_C = 244°C$ and $\Delta T_B = 6°C$.

For the model with the functionally graded material sandwiched between the ceramic and bond coatings, the thermal conductivity K_G of the FGM can be assumed to be a function of z, $K_G(z)$. Therefore, the heat flux across the coatings with FGM can be expressed as:

$$q = -K_B k_1 = -K_G(z)\left(\frac{dT}{dz}\right)_G \qquad (8)$$

Suppose $K_G(z)$ varies linearly with z, $K_G(z) = a + bz$ where $a = K_C - t_C(K_B - K_C)/t_G$, $b = (K_B - K_C)/t_G$. From (8), the temperature ΔT_G in the FGM (measured from the interface of the ceramic coating and FGM) is:

$$\Delta T_G = \int_{t_C}^{z} \frac{K_B k_1}{K_G(z)}\,dz = \frac{K_B k_1}{b}\ln\left(\frac{a+bz}{a+bt_C}\right) \qquad (9)$$

If we let $z = t_C + t_G$ in (9), the temperature increment in the FGM is $\Delta T_G = 2.902 k_1 t_G$. The temperature increments in the bond and ceramic coating are $\Delta T_B = k_1 t_B$ and $\Delta T_C = 15 k_1 t_C$, respectively. Here we used $t_B = 0.08$ mm, $t_G = 0.1$ mm and $t_C = 0.35$ mm.

Since $\Delta T = 250°C$ and $\Delta T = \Delta T_C + \Delta T_G + \Delta T_B$, the constant k_1 can be evaluated as $44.48°C/mm$. Then, the temperature can be evaluated as $\Delta T_B = 3.6°C$, $\Delta T_G = 12.9°C$, $\Delta T_C = 233.5°C$.

5.2. Temperature profiles inside crack region

When the insulation effect across the crack faces is included, the temperature variation through thickness becomes discontinuous. In the following sections, the temperature fields above and below the crack faces or inside the crack region are derived for three different crack locations.

5.2.1. Crack on ceramic-bond coating interface.
First, we consider a crack on the ceramic–bond coating interface. In order to determine the temperature distribution, the previous derivation shown in Section 5.1 is extended to include the temperature jump across the crack faces. The

temperature drops in the ceramic and bond coatings are still linear functions of z and the heat flux in these coatings can be expressed as,

$$q = \frac{T_{env} - T_1}{t_C} K_C = \frac{T_2 - T_{sub}}{t_B} K_B \qquad (10)$$

where T_{env} is the environment temperature, T_{sub} is the substrate temperature, T_1 is the temperature on the upper crack surface and T_2 is the temperature on the lower crack surface. The temperatures at these key locations are noted in Fig. 10(a). The heat flux across the crack can be expressed as,

$$q = (T_1 - T_2)h_C \qquad (11)$$

where h_C is the gap conductance across crack faces. A higher gap conductance h_C implies less insulation or temperature jump. If $h_C = \infty$, no thermal insulation exists and the temperature remains
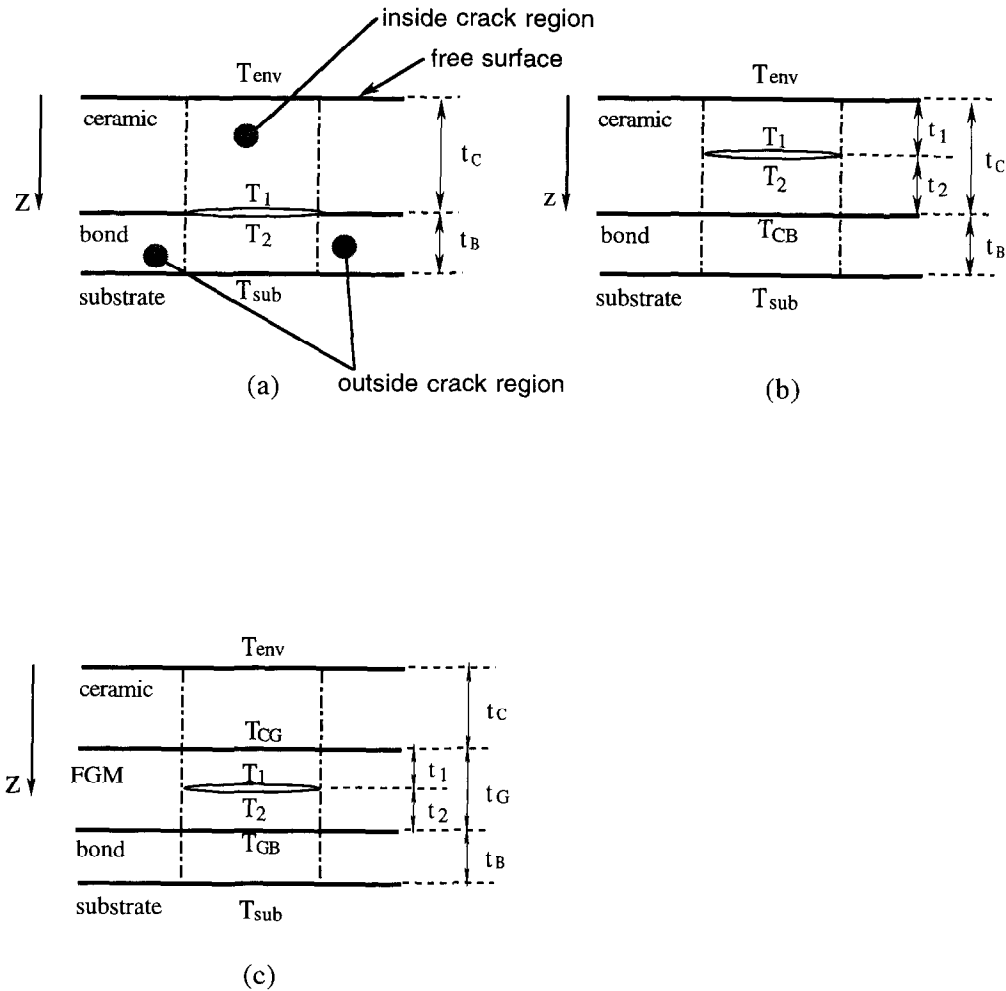

Fig. 10. Cross-sectional models used to determine temperature distributions within the coatings. The temperatures at key boundaries are noted. For each model, two separate temperature distributions are assumed. One for the inside crack region where the temperature jump across the crack faces is modeled, and the other for the outside crack region where the temperature change through thickness is always continuous. (a) Interface crack between the ceramic and bond coatings. (b) Homogeneous crack within the ceramic coating. (c) Crack in the functionally graded material.

continuous across the crack faces. Alternatively, $h_C = 0$ corresponds for perfect insulation and we have $T_{env} = T_1$ and $T_2 = T_{sub}$. The thermal insulation of crack faces can also be expressed in terms of the Biot number B_C. This parameter was effectively used in the homogeneous coating analysis [23] and ranges $0 \leqslant B_C \leqslant \infty$. In order to utilize the Biot number in the bimaterial crack, an effective Biot number B_C^* is introduced as,

$$\frac{2}{B_C^*} = \frac{1}{B_C^C} + \frac{1}{B_C^B} \tag{12}$$

where $B_C^C = h_C t / K_C$, $B_C^B = h_C t / K_B$ where t is the total thickness of the coating. Using the Biot numbers, we can solve for T_1 and T_2 from (10) and (11) as,

$$T_1 = \frac{1}{1 + \eta + B_C^B + \eta B_C^C} [(1 + \eta + B_C^B) T_{env} + \eta B_C^C T_{sub}],$$

$$T_2 = \frac{1}{1 + \eta + B_C^B + \eta B_C^C} [B_C^B T_{env} + (1 + \eta + \eta B_C^C) T_{sub}] \tag{13}$$

where η is the ratio of the thickness of the ceramic coating to the thickness of the bond coat. It can be verified that (13a) and (13b) reduce to the expressions given for a homogeneous crack shown in [23].

5.2.2. Crack within ceramic coating. For a crack located inside the surface ceramic coating, T_1 and T_2 can be derived from (13) by letting $B_C^B = B_C^C$ since the crack is homogeneous. But the substrate temperature T_{sub} in (13) must be replaced by T_{CB} which is the temperature at the ceramic–bond interface. Also, we denote t_1 to be the thickness of the ceramic coating above the crack and t_2 to be the thickness below the crack, so that $t_C = t_1 + t_2$ as shown in Fig. 10(b). The heat flux equation for this case is given by

$$q = \frac{T_2 - T_{CB}}{t_2} K_C = \frac{T_{CB} - T_{sub}}{t_B} K_B \tag{14}$$

By substituting (14) into (13) where T_{sub} is replaced by T_{CB} and $B_C^C = B_C^B$, T_2 can be determined. Also T_1 and T_{CB} can be determined as

subsections. Also T_{CG} and T_{GB} are the temperatures at the ceramic–FGM interface and FGM–bond interface, as shown in Fig. 10(c). The heat flux equations in the bond coat and that across the crack in the FGM can be shown as,

$$q = (T_1 - T_2) h_C = k_1 K_B \tag{16}$$

which gives $T_1 - T_2 = k_1 K_B / h_C$. The temperature drop in the FGM can be evaluated from (9) as,

$$\Delta T_G = T_1 - T_2 + \frac{k_1 K_B t_G}{K_C - K_B} \ln\left(\frac{K_C}{K_B}\right) \tag{17}$$

Note that the integration in (9) is carried out continuously across the entire thickness of FGM, which leads to the last term in (17). Thus, the slope k_1 can be evaluated as

$$k_1 = \Delta T \left[t_B + \frac{K_B}{K_C} t_C + \frac{K_B}{K_B - K_C} \ln\left(\frac{K_B}{K_C}\right) t_G + \frac{K_B}{h_C} \right]^{-1} \tag{18}$$

With k_1 known, the temperature distribution in the coatings with a FGM can be determined. The temperatures at the key locations are

$$T_{CG} = T_{env} - \frac{k_1 K_B}{K_C} t_C$$

$$T_1 = T_{CG} - \frac{k_1 K_B}{b} \ln\left[\frac{a + b(t_C + t_1)}{a + b t_C}\right]$$

$$T_2 = T_1 - \frac{k_1 K_B}{h_C}$$

$$T_{GB} = T_{sub} + k_1 t_B \tag{19}$$

where a and b are given in Section 5.1. The temperatures inside the bond and ceramic coatings can be calculated by linearly interpolating between the temperatures at the end cross sections. The temperature distribution inside the FGM follows the logarithm formula (9).

$$T_1 = \frac{1 + \eta + B_C}{(1 + \eta)(1 + B_C)} T_{env} + \frac{\eta B_C \kappa \gamma}{(1 + \eta)(1 + B_C)(1 + \kappa \gamma)} T_{sub} + \frac{\eta B_C}{(1 + \eta)(1 + B_C)(1 + \kappa \gamma)} T_2$$

$$T_2 = \frac{(1 + \eta)(1 + B_C)(1 + \kappa \gamma)}{(1 + \eta)(1 + B_C)\kappa \gamma + B_C} \left[\frac{B_C}{(1 + \eta)(1 + B_C)} T_{env} + \frac{(1 + \eta + \eta B_C)\kappa \gamma}{(1 + \eta)(1 + B_C)(1 + \kappa \gamma)} T_{sub} \right] \tag{15}$$

$$T_{CB} = \frac{\kappa \gamma T_{sub} + T_2}{1 + \kappa \gamma}$$

where $\eta = t_1/t_2$, $\gamma = t_2/t_B$, $\kappa = K_B/K_C$, $B_C = h_C t_C/K_C$.

5.2.3. Crack in functionally graded material (FGM). The effect of thermal insulation of a crack in the FGM is now considered. Here, T_{env}, T_{sub}, T_1 and T_2 have the same definitions as in the earlier two

5.3. Effects of CTE mismatch—without thermal insulation across crack

For the finite element calculation, the steady state solutions determined in the previous sections are

prescribed as the temperature field. The energy release rate and the mixed-mode stress intensity factors are computed using (1) and (5) with the thermal stress terms for various crack locations. First, the analysis is carried out without modeling the thermal insulation across the crack faces. Under this condition, the energy release rate goes up very rapidly with increasing crack radius (figures are not shown).

However, its magnitude remains very small for all cases. At $a = 3$ mm, G ranges from 0.2 to 1.6×10^{-3} J/m^2, which is substantially less than the critical energy release rate found in the experiment in Section 4. The effect of FGM is also insignificant under this condition. Additional computations have also revealed that most of the energy release rate is generated by the temperature gradient through thickness and not by the CTE mismatch of different layers.

5.4. Effects of thermal insulation across crack faces

In the previous section, the crack is assumed to have no effects on the heat flux, and the heat conduction across the crack is assumed to be continuous. However, in real TBCs, opened cracks have air entrapped between the free crack surfaces, which may act as an effective shield against the heat flux. Alternatively, the thermal insulation, namely the discontinuity of temperature across the crack faces (i.e., a temperature jump from the upper to lower surfaces), should be observed if the crack size is at least comparable to the coating thickness. When a large temperature jump between the regions above and below the crack exists, the crack tip deformation is more distorted and expected to produce a higher energy release rate. Such a condition should increase the likelihood of the TBC failure in a high temperature environment. Here, the crack driving force of the following three models is investigated.

In Fig. 11(a), the temperature profiles through thickness of the interface crack between the ceramic and bond coatings are determined from (13) and shown for various effective Biot numbers. For a typical crack in a TBC, the Biot number is expected to be of order unity and it decreases with larger crack opening [23]. The effective Biot number indicates the magnitude of the crack face insulation. For $B_c^* < \infty$, there is a temperature jump across the crack faces at $z = 0.4$ mm. Outside the crack region, the temperature variation is always continuous and the profile is identical to the one shown for $B_c^* = \infty$. The energy release rate for various crack radii for this model is shown in Fig. 10(b). The magnitude of G is quite significant even in a model with relatively small temperature jump across crack faces. We note that the results with small radius ($a < 0.2$ mm) may be inaccurate since the present study does not model precise temperature distribution near the crack front.

The temperature distributions with different degrees of crack face insulation are shown in Fig. 12(a) for the homogeneous crack within the ceramic
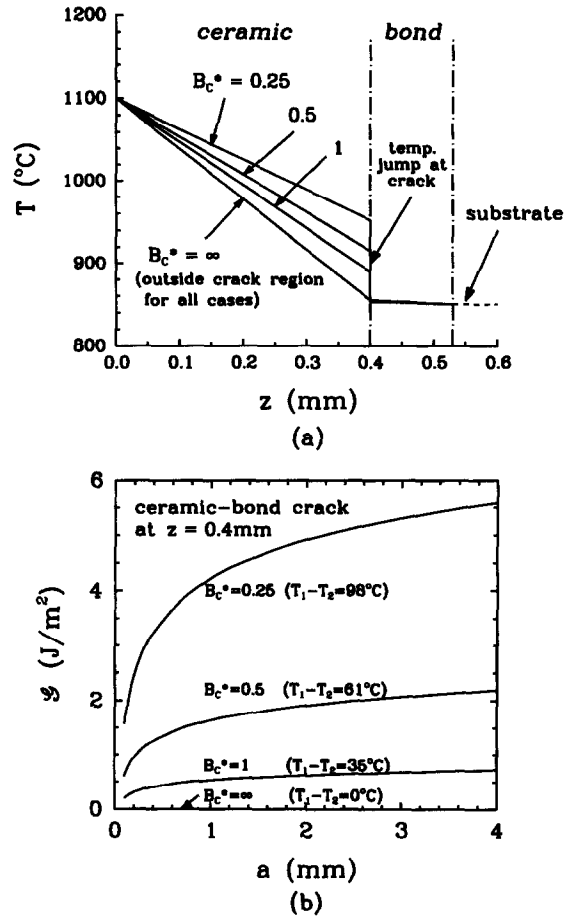

Fig. 11. (a) Temperature profile inside the crack region of the ceramic–bond interface crack model. The effective Biot numbers B_c^* are noted for different temperature jumps across the crack surfaces. For each case, the temperature profile outside the crack region is always given by the $B_c^* = \infty$ profile. (b) Energy release rate as a function of embedded crack radius for different temperature jumps across the crack surfaces. The result for $B_c^* = \infty$ (no temperature jump) is extremely small.

coating at $z = 0.2$ mm. The temperature jump increases with decreasing Biot number. The calculated energy release rate is shown in Fig. 12(b). Again, the values are very high and comparable to the toughness of the ceramic layer found earlier (i.e., $G = 1.0$ J/m^2). In fact, when $B_c = 2$ and $T_1 - T_2 = 82°C$, the resulting energy release rate is well above the critical value except for very small cracks.

For the crack within the FGM, the temperature distributions determined from (19) are shown in Fig. 13(a) for various Biot numbers. The corresponding energy release rate shown in Fig. 13(b) has similar trends as in the other cases.

In Fig. 14(a), the energy release rate is plotted as a function of $T_1 - T_2$ for the three crack locations. The results are shown for a fixed crack radius, $a = 1$ mm. In all cases, the increase of G is quite
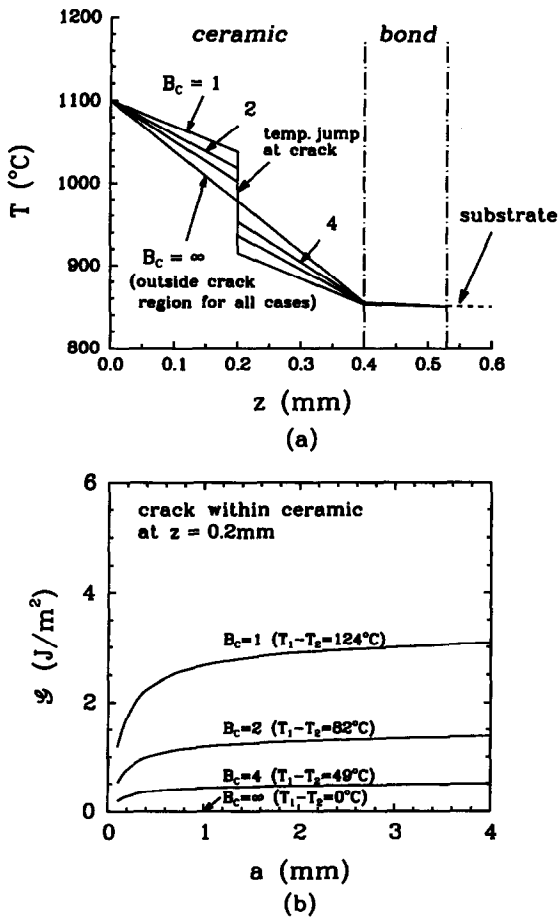
Fig. 12. (a) Temperature profile inside the crack region of the ceramic crack model. The Biot numbers B_C are noted for different temperature jumps across the crack surfaces. (b) Energy release rate as a function of embedded crack radius for different temperature jumps across the crack surfaces.

significant when any insulation across the crack faces is considered. It is interesting to note that the crack in the FGM has the highest G for a given $T_1 - T_2$. The phase angles are shown in Fig. 14(b). In all cases, the phase angles reach steady state when $T_1 - T_2 = 10°C$. Most importantly, the calculated phase angles indicate even greater K_{II} with respect to K_I, i.e., very large shear loading in the crack tip region.

6. CONCLUSIONS

A simple but effective fracture toughness test method, which is consistent with the mixed-mode fracture mechanics theory, is introduced. The current method closely models actual TBCs where embedded flaws or voids may act as the source of failure and crack growth initiation. The axisymmetrical geometry also eliminates any ambiguity associated with the 3-D effects in previous fracture tests. The biggest advantage of this method lies in the simplicity of

experimental procedure. It requires very little additional set-up over the common tensile adhesion test.

From a detailed finite element analysis, we have found accurate crack driving forces and stress intensity factors under various geometrical conditions. Recent fracture experiments have shown that the mode-mix, or the phase angle as described here, play a significant role in determining the fracture toughness measured in terms of energy release rate. In general, a larger critical energy release rate has been observed in a loading condition with relatively greater shearing load. This effect is studied carefully in the current analysis for TBCs under tensile load and high temperature environment. The simulations of thermally loaded coatings have also clarified the roles of the material mismatch, the temperature gradient through thickness and the thermal insulation across the crack faces.

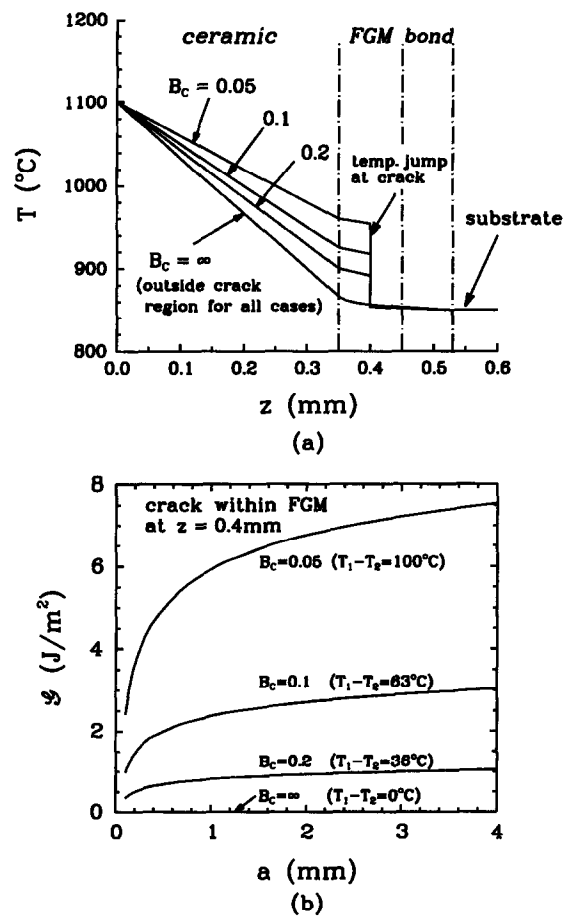Key observations from the present combined

Fig. 13. (a) Temperature profile inside the crack region of the FGM crack model. The Biot numbers B_C are noted for different temperature jumps across the crack surfaces. (b) Energy release rate as a function of embedded crack radius for different temperature jump across the crack surface.
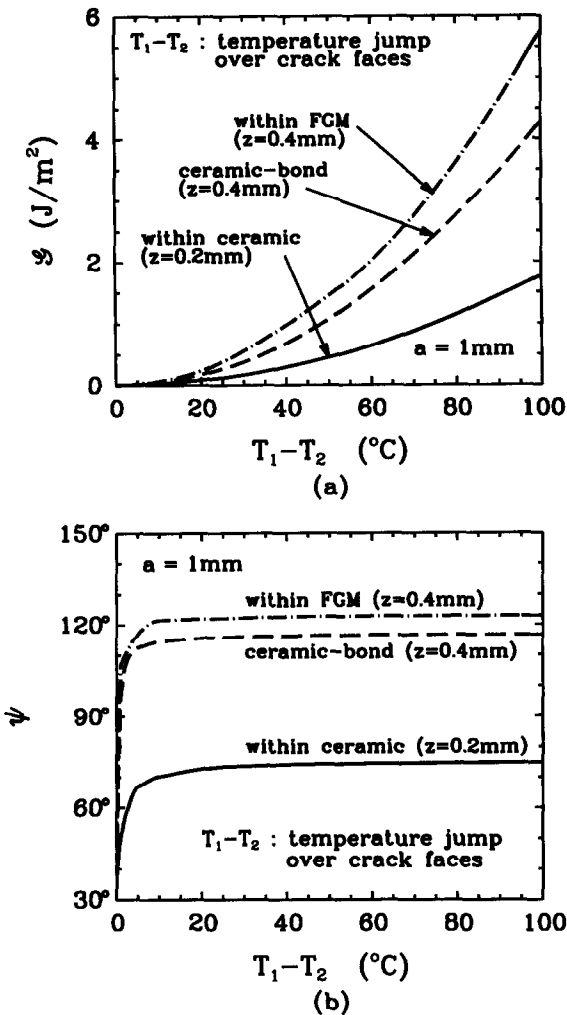
Fig. 14. (a) Energy release rate as a function of temperature jump across the crack faces. The results are shown for cracks at various locations. In all cases, the radius is $a = 1$ mm. (b) Corresponding phase angle.

- In high temperature environments, the effects of bimaterial mismatch and the temperature gradient are found to be small while the effect of thermal insulation across crack faces can be very large. This effect probably controls the crack growth initiation within ceramic coatings.
- The functionally graded material may not directly benefit the integrity of coatings since the material mismatch does not play a significant role in high temperature environments and the interface of ceramic and bond coatings is substantially tougher than the ceramic coat itself. Its effectiveness in the high temperature application may need to be re-evaluated.

Further testing of TBCs is planned in the near future to accumulate more experimental data. It is important to measure the critical energy release rate under a loading condition which is similar to the one in a high temperature environment. From our tensile test, we determined $G_c = 1.0$ J/m^2 when $\psi = -6.5°$ for the ceramic coating. However, the high temperature analysis predicts the mixed-mode state of $\psi = 70°$ for an embedded crack. In order to determine a more relevant toughness of TBCs, one needs to find G_c at this phase angle. An adhesion fracture testing under such a phase angle may be possible by increasing the thickness of the epoxy layer as discussed in Section 3.3. This aspect will be carefully investigated in the future work.

experimental and computational analysis can be summarized as below.

- Failure of the TBC always occurs in the ceramic surface coating due to its lowest fracture resistance over other materials and interfaces in the coatings. Any strengthening of the TBC must involve fracture toughness improvement of the ceramic layer.
- The application of an adhesive epoxy layer must be carried out carefully since it significantly affects the energy release rate as well as the tensile to shear ratio in the crack front region.
- The mixed-mode state or the phase angle in the tensile fracture test is dominantly tensile while that of the high temperature environment is dominantly shear. This implies that the fracture test of TBC probably underestimates the critical energy release rate of the coatings under thermal loading conditions.

REFERENCES

1. C. H. Liebert and R. A. Miller, Ind. Eng. Chem. Prod. Res. Dev. 23, 344 (1984)
2. H. Herman, Scientific American 256, 9–112 (1988).
3. H. Herman and N. R. Shankar, Mater. Sci. Eng. 88, 69 (1987).
4. K. T. Scott and R. Kingswell, in Advanced Surface Coatings (edited by D. S. Rickerby and A. Matthews), p. 217. Chapman and Hall, New York (1991).
5. J. Weber, Welding J. 71, 3–93 (1992).
6. S. Moore and G. Samdani, Chem. Eng. 100, 39 (1993).
7. ASTM 633–79, American Society of Testing Materials, Philadelphia (1979).
8. C. K. Lin and C. C. Berndt, J. Therm. Spray Tech. 3, 75 (1994).
9. J. S. Wang and Z. Suo, Acta Met. 38, 1279 (1990).
10. H. C. Cao and A. G. Evans, Mech. Mater. 7, 295 (1989).
11. W. Han, E. F. Rybicki and J. R. Shadley, in Thermal Spray Coating: Research, Design and Application (edited by C. C. Berndt and T. F. Bernecki), p. 55 (1993).
12. S. H. Leigh, C. C. Berndt, C. L. Wu and T. Nakamura, in Thermal Spray Industrial (edited by C. C. Berndt and S. Sampath), p. 655 (1994).
13. T. E. Strangman, J. Neumann and A. Liu, Thermal

Barrier Coating Life Prediction Model Development, Final Report, NASA CR-179648 (1987).

14. C. F. Shih, B. Moran and T. Nakamura, *Int. J. Frac.* **30**, 79 (1986).

15. G. Qian, Master Thesis, State Univ. of New York at Stony Brook, New York (1995).

16. J. Rice, *J. appl. Mech.* **55**, 98 (1988).

17. J. R. Rice, Z. Suo and J. S. Wang, in *Metal–Ceramics Interfaces* (edited by M. Ruhle *et al.*), pp. 269–294. Pergamon Press, Oxford (1990).

18. R. Nahta and B. Moran, *Int. J. Solids Struct.* **30**, 2027 (1993).

19. F. Delale and F. Erdogan, *J. appl. Mech.* **55**, 317 (1988).

20. M. Y. He and J. W. Hutchinson, *J. appl. Mech.* **56**, 270 (1989).

21. K. Kokini, *J. Am. Ceram. Soc.* **70**(12), 855 (1987).

22. K. Kokini and B. D. Choules, *Composite Engin.* **5**, 865 (1995).

23. J. W. Hutchinson and T. J. Lu, *J. Eng. Mater. Tech.* **117**, 386 (1995).

24. *Thermophysical Properties of Matter—Thermal Conductivity* (edited by Y. S. Touloukian *et al.*), **1** and **2**, IFI/Plenum, New York-Washington (1970).